JOURNAL OF MATERIALS SCIENCE **38** (2003) 643–655

Synthesis and structural and optical properties of metastable ZrO_2 nanoparticles with intergranular Cr^{3+}/Cr^{4+} doping and grain surface modification

S. RAM
Materials Science Centre, Indian Institute of Technology, Kharagpur 721 302, India
E-mail: sram@matsc.iitkgp.ernet.in

Nanoparticles of stabilized ZrO_2 in a single cubic (c) phase are obtained with an intergranular doping of 4 to 20 at.% Cr^{3+}/Cr^{4+} additives by a chemical method using a high energy amorphous precursor with polymer molecules of sucrose and polyvinyl alcohol. In the polymer, the metal cations disperse and rearrange in a specific network structure with local symmetry probably similar to that in c-ZrO_2. On heating at 250 to 800°C in air, the polymer network decomposes and burns out spontaneously (with a strong exothermic peak over 350 to 500°C in thermal analysis) in a refined microstructure in 10 to 20 nm diameter particles of near spherical shape. Those are identified to be of c-ZrO_2 by x-ray diffraction. A modified microstructure of 15 to 30 nm crystallites of dispersed tetragonal (t) and/or monoclinic (m) phases in stabilized c-ZrO_2 develops on a prolong heating at 900 to 1000°C from a polymer precursor for 2 h or longer. Particles in t-ZrO_2 are in acicular shape, as long as 450 nm with aspect ratio $\phi \sim 5$ to 20, while in the shape of platelets in m-phase in an average 300 nm size. It is found that the Cr^{3+}/Cr^{4+} additives promote formation of c-ZrO_2 by a controlled decomposition and combustion of precursor in small particles at 250 to 800°C temperature. Part of the additives form a thin amorphous surface layer in individual c-ZrO_2 grains so that it prevents them to grow or transform in the equilibrium m-ZrO_2 bulk structure as long as the temperature lies below 900°C. The x-ray diffraction in light of the optical spectrum reveals that part of the Cr^{4+} cations occupy Zr^{4+} sites in a distorted c-ZrO_2 lattice.

1. Introduction

Bulk ZrO_2 at ambient pressure is polymorphic, exhibiting *Fm*3*m* cubic (c) fluorite structure at high temperatures above 2370°C, $P4_2/nmc$ tetragonal (t) structure at intermediate 1200 to 2370°C temperatures, and $P2_1/c$ monoclinic (m) structure at low temperatures below 950°C [1–5]. The transformation from the m- to t- or c-ZrO_2 polymorph is reversible so the high temperature polymorphs do not retain on cooling to room temperature [1, 2]. At high pressure, it adopts *Pbca* and *Pnam* two orthorhombic structures [2]. A third $Pbc2_1$ orthorhombic form is observed in few examples of partially stabilized ZrO_2 [6, 7].

The different ZrO_2 polymorphs have their own intrinsic physical and chemical properties, which make them to be of the most important engineering materials. High hardness, high wear resistance, low coefficient of friction, high elastic modulus, chemical inertness, good ionic conductivity, low thermal conductivity, and high melting temperature are their common properties [8, 9]. A displacive t → m phase transformation, which occurs at ∼950°C with a shear strain of ∼0.16 and a volume expansion of ∼4% on cooling from a high temperature [1, 2], limits applications of m-ZrO_2 as refractory or other engineering materials. It invokes a catastrophic fracture [2]. It can be resolved if replacing m-phase by the other phases. Efforts have been made to stabilize them in small crystallites of size at a nanometer scale with dopants of MgO, CaO, Y_2O_3, CeO_2, Mg_3N_2, Si_3N_4, AlN, etc. [8–13]. Spray pyrolysis [14], vapor phase hydrolysis [13], hydrothermal process [12], gas condensation [15], sol-gel process [16], and combustion methods [17] are explored in order to control a refined microstructure with a uniform distribution of additives in thin ZrO_2 grain surface layers.

As such Cr^{3+} is hardly soluble in ZrO_2 in a significant amount to stabilize in c- and t-phases by a conventional method [18–21]. ZrO_2 admixed with Cr_2O_3 has applications of catalytic uses in production of H_2 by H_2O dissociation, in producing H_2 and carboxylic acids from water and aldehyde, in decomposition of $CHClF_2$, in production of green chromophores [20, 21], and as a potential conductor in magneto-hydrodynamic generators [18, 20]. Stabilized c-ZrO_2 is specially used as oxygen sensor [16], solid fuel cells [22], ceramic components [19] and as catalyst or catalyst promoter in synthesizing alcohol by hydrogenation of CO [20]. It has plenty of oxygen vacancies to act as active sites in catalytic activity [23].

A partially stabilized or a multiphase ZrO_2 forms transformation toughened composites [1, 2]. A fine-scale precipitate of m-ZrO_2 and/or t-ZrO_2 in a stabilized c-ZrO_2 matrix improves toughness [1]. It gives a new strengthening mechanism in composites by a strong macroscopic interaction between components [1, 24].

In this article, we report synthesis of Cr^{3+}/Cr^{4+} stabilized c-ZrO_2 nanoparticles with a new chemical method [25] with dispersed metal cations in a polymer of sucrose and polyvinyl alcohol (PVA). Dispersed Cr^{3+}/Cr^{4+} cations with polymer molecules easily dissolve in a sufficient amount up to 30 at.% (of the total metal cations) in an amorphous precursor structure of Zr^{4+} cations. Stabilized c-ZrO_2 nanoparticles appear on a reconstructive decomposition and combustion of precursor at temperature as low as 250°C. A modified microstructure develops of dispersed t-and/or m-phase(s) in c-ZrO_2 at 900 to 1050°C. The results are presented with structural and optical studies of the specimens. Substantially stable c-ZrO_2 forms and exists in small particles in support of an intergranular amorphous phase with a thin molecular grain surface layer of the Cr^{3+}/Cr^{4+} additives.

2. Experimental details

2.1. Synthesis

A polymer precursor with dispersed Zr^{4+} and Cr^{3+}/Cr^{4+} cations in a specific ratio is obtained by reaction of analytical grade (i) $ZrO(OH)_2 \cdot xH_2O$, (ii) $(NH_4)_2Cr_2O_7$, (iii) sucrose, and (iv) PVA. A freshly prepared $ZrO(OH)_2 \cdot xH_2O$ by hydrolysis of $ZrO(Cl)_2 \cdot 8H_2O$ with NH_4OH in an aqueous solution is used. The hydrolysis reaction follows as

$$ZrOCl_2 + (2 + x)H_2O \rightleftharpoons ZrO(OH)_2 \cdot xH_2O + 2H^+ + 2Cl^- \quad (1)$$

According to it, both the $2H^+$ and $2Cl^-$ ion concentrations are as large as twice the initial concentration, which was ~0.5 mol/dm^3 (1 dm^3 = 1 L), in $ZrO(Cl)_2 \cdot 8H_2O$ solution. The reaction proceeds if they react. NH_4OH thus has been added drop wise in order to probe the influence of the $2H^+$ and $2Cl^-$ ions produced by the hydrolysis on the formation processes of $ZrO(OH)_2 \cdot xH_2O$ in an amorphous structure. It reacts with HCl and forms NH_4Cl, which is soluble in water and thus goes to the solution. Average ionic strength of the solution with $ZrO(OH)_2 \cdot xH_2O$ sol or gel thus way does not increase much to govern a controlled reaction in cold water at room temperature. As soon as the $ZrO(OH)_2$ molecules appear recombine one another via oxobridging in an amorphous structure in association with H_2O molecules.

As summarized in Fig. 1, the recovered $ZrO(OH)_2 \cdot xH_2O$ sample was washed in distilled water and then pulverized and dissolved in nitric acid in a 0.5 mol/dm^3 solution. Cr^{6+} cations were added in a predetermined ratio through an aqueous $(NH_4)_2Cr_2O_7$ solution in 0.5 mol/dm^3 concentration with a continuous magnetic stirring. Addition of sucrose and PVA (mol. wt. 1,25,000) by 50 to 70% in a batch of 25 g sample yields a final polymer precursor solution in a transparent light green color. A 13:1 molar ratio is maintained in sucrose and PVA polymers. It prevents unwanted phase separation in metal cations.

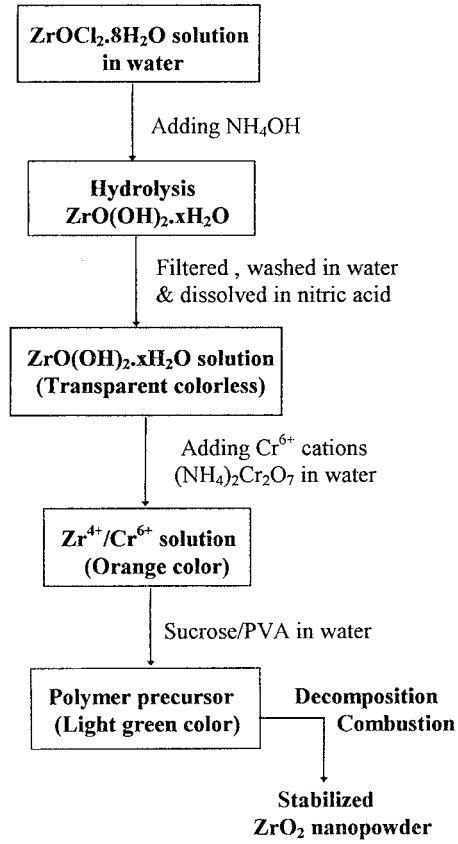

Figure 1 Schematic diagram of forming a polymer precursor with metal cations in an aqueous sucrose-PVA solution and its decomposition to ZrO_2 nanopowder.

The obtained solution is dried into a precursor mass in a dark black characteristic color by evaporating the excess water over a water bath (of Julabo model HD-4) at 50 to 80°C. The latter is pyrolysed into a fluffy powder in a light brown to deep blue color, depending upon the Cr^{3+}/Cr^{4+} content, by heating over a hot plate at 250°C in air. A further calcination at 600 to 900°C results in a stabilized ZrO_2 nanopowder. A series of samples with Cr^{3+}/Cr^{4+} contents up to 30 at.% thus have been obtained after calcining from the amorphous polymer precursor mass at representative temperatures between 250 and 1050°C in air.

2.2. Characterization and measurements

Thermal decomposition and *in situ* combustion of polymer precursor mass into a refined ZrO_2 powder are studied with thermogravimetric analysis (TG) and differential thermal analysis (DTA) by heating the specimen at 5°C/min in a thermal analyzer (Model DT-40, Shimadzu Co. Kyoto, Japan). Phase analysis is carried out with x-ray diffraction of representative samples with the help of a Philips PW-1804 x-ray powder diffractometer with filtered Cu Kα radiation of $\lambda = 0.15418$ nm wavelength.

Average crystallite size d is calculated from width $\Delta 2\theta_{1/2}$ in characteristic peaks with the Debye Scherrer

relation [26]. Specific surface area in particles is studied with N_2 gas adsorption with BET measurements [27]. Size and morphology of crystallites and particles, or the clusters of small crystallites, in powder are studied with a scanning electron microscope (SEM) of JEOL model JSM-5800 and a transmission electron microscope (TEM) of model-JEM 2000 CX. The final chemical compositions of Cr^{3+}/Cr^{4+} modified ZrO_2 samples are confirmed by *in situ* EDX analysis with SEM micrographs in conjunction with an energy dispersive x-ray spectrum analyzer. The sample in TEM analysis was prepared by dispersing powder in alcohol over an ultrasonic bath. A drop of suspension was carefully placed with a syringe on a carbon coated Formvar film predeposited on a copper grid, which was ultimately loaded with sample in the microscope for the analysis.

The presence of Cr^{3+} and Cr^{4+} are analyzed in the stating polymer precursor as well as in the derived ZrO_2 nanopowders by their chemical tests [28]. This is further analyzed and confirmed by their electronic absorption spectra. The absorption spectrum (190 to 700 nm region of the electromagnetic spectrum) is measured of powder dispersed in a thin layer (of 2 to 10 μm thickness) over a transparent optical quartz plate with an uv-visible (Shimadzu UV-3100) spectrophotometer.

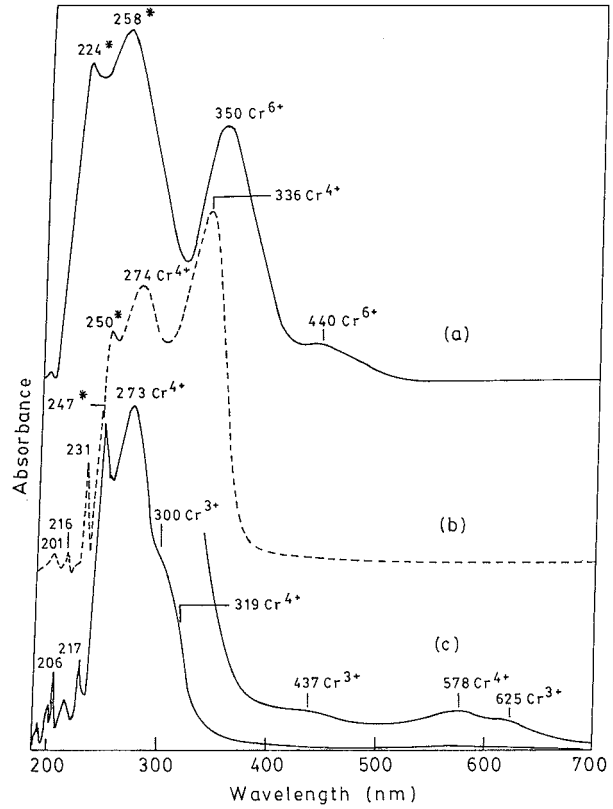

Figure 2 Electronic absorption spectra in (a) Cr^{6+} in 0.0002 M $(NH_4)_2Cr_2O_7$ in water and that of transformed into Cr^{4+} and Cr^{3+} after adding 2 vol% of (b) sucrose or (c) PVA in 10% solution in water. *Charge transfer bands.

3. Results and discussion

3.1. Reaction process in formation of polymer precursor

As demonstrated in Fig. 1, the addition of sucrose followed by PVA (dissolved in water) to a transparent mixed solution (say A) of $Zr(OH)_4 \cdot xH_2O$ and $(NH_4)_2Cr_2O_7$ in a specific ratio results in a specimen of dispersed metal cations in a polymer matrix of sucrose and PVA polymer molecules. The sucrose reacts with $(NH_4)_2Cr_2O_7$ in the solution and reduces its oxidation state of chromium $Cr^{6+} \rightarrow Cr^{4+}/Cr^{3+}$ with a change of its initial color from orange to a light green one. The light green equilibrium color becomes stable at a stable $Cr^{4+} \Leftrightarrow Cr^{3+}$ configuration in the polymer as per the experimental conditions. A similar change in color also appears on a reaction of PVA with solution A but that reverts in a characteristic light orange color within a period of 5 to 10 h of the reaction in cold water at room temperature.

A characteristic orange color in $(NH_4)_2Cr_2O_7$ occurs in a ligand-metal ($L \rightarrow Cr^{6+}$) charge transfer band otherwise $Cr^{6+}(3d^0)$ has no spectrum in this region. Here, the ligand L is formed by O^{2-} anions surrounding the Cr^{6+} cations. The original Cr^{6+} oxidation state is thus reduced to Cr^{4+} or Cr^{3+} on dispersing in sucrose or PVA polymer molecules in water. This is analyzed by a chemical test as follows. In a 20 ml of $(NH_4)_2Cr_2O_7$ solution (with PVA or sucrose) in water is added 0.1 g of KI followed by 5.0 ml CH_3COOH in a beaker. The sample is covered with a watch glass, to avoid its oxidation with air, and stirred for a few min to let the iodide oxidize by Cr^{4+} in the sample as per the $I^- + Cr^{4+} \rightarrow I_2 + Cr^{3+}$ reaction. The I_2 turns color of the sample from light green into a violet, which changes in an intense blue color if adding starch. The blue color disappears instantaneously on adding sodium thiosulphate, reduces iodine to iodide, $I_2 + S_2O_3^{2-} \rightarrow I^- + S_4O_6^{2-}$, again. The intense blue color in the so called "charge transfer band" disappears as the I_2-starch complex breaks down.

The electronic absorption spectra of Cr^{6+}: $(NH_4)_2Cr_2O_7$ before (a) and after adding (b) sucrose or (c) PVA (Fig. 2) in the acidic solution in water confirm the transformation of Cr^{6+} to (b) Cr^{4+} or (c) Cr^{4+}/Cr^{3+}. As summarized in Table I, two

TABLE I The electronic absorption bands in modified $Cr^{6+} \rightarrow Cr^{4+}/Cr^{3+}$ oxidation state in $(NH_4)_2Cr_2O_7$ dissolved in sucrose and PVA polymer in water

Band positions (nm)			
$(NH_4)_2Cr_2O_7$	$(NH_4)_2Cr_2O_7$ in sucrose	$(NH_4)_2Cr_2O_7$ in PVA	Transitions
		625 (vw)	$^4A_{2g} \rightarrow {}^2E_g$ (Cr^{3+})
		578 (vw)	$^3T_1 \rightarrow {}^3A_2$ (Cr^{4+})
440 (vw)	–	–	$^1A_{1g} \rightarrow {}^1T_{2g}$ (Cr^{6+})
	–	437 (vw)	$^4A_{2g} \rightarrow {}^4T_{2g}$ (Cr^{3+})
350 (ms)	–	–	$^1A_{1g} \rightarrow {}^3A_{2g}$ (Cr^{6+})
	336 (vs)	319 (w)	$^3T_1 \rightarrow {}^3T_1$ (Cr^{4+})
	–	300 (ms)	$^4A_{2g} \rightarrow {}^4T_{1g}$ (Cr^{3+})
	274 (s)	273 (vs)	$^3T_1 \rightarrow {}^3T_2$ (Cr^{4+})
258 (vs)	250 (ms)	247 (vs)	
224 (s)	–	–	Charge transfer bands
	231 (vw)	–	
	216 (vw)	217 (vw)	Vibronic bands
	201 (vw)	206 (vw)	

The relative intensities in the bands are given in the parentheses; vs: very strong, s: strong, ms: medium strong, w: weak, and vw: very weak intensity values.

bands at 440 and 350 nm in spectrum (a) are in $^1A_{1g} \rightarrow {}^3A_{2g}$ and $^1A_{1g} \rightarrow {}^1T_{2g}$ electronic transitions of $Cr^{6+}(3d^0)$ [28, 29]. Other two bands, which appear at much lower λ (or higher energy) at 258 and 224 nm, are the $L \rightarrow Cr^{6+}$ charge transfer bands which occur through a ligand with O^{2-} anions [28]. The bands due to $Cr^{4+}(3d^2)$ are developed at 336 nm ($^3T_1 \rightarrow {}^3T_1$) and 274 nm ($^3T_1 \rightarrow {}^3T_2$) in spectrum (b) and those are shifted at 319 nm and 273 in spectrum (c). A third band in Cr^{4+} ($^3T_1 \rightarrow {}^3A_2$) has developed at 578 nm in spectrum (c). Bands from Cr^{3+} ($3d^3$) in spectrum (c) are observed at 625 nm ($^4A_{2g} \rightarrow {}^2E_g$), 437 nm ($^4A_{2g} \rightarrow {}^4T_{2g}$), and 300 nm ($^4A_{2g} \rightarrow {}^4T_{1g}$). All the transitions except the $^4A_{2g} \rightarrow {}^2E_g$ in Cr^{3+} are spin allowed and thus appear with a large intensity. An easier 3d–3d excitation in Cr^{3+} with three free 3d electrons occurs in the bands at lower energy in comparison to those in Cr^{4+} with a lesser number of only two free 3d electrons. The sharp (and weak) bands observed between 250 and 200 nm in spectra (b) and (c) are possibly vibronic bands.

Sucrose and PVA forms a polymer with dispersed metal cations in water. Here, sucrose plays a multifunctional role. At first, it forms a complex with metal cations by coordinating through hydroxyl groups in small micelles. The micelle circumvents selective precipitation of encapsulated cations within it while evaporating the excess water in the solution to a dried precursor mass. Sucrose, being in excess to the cations, behaves as a strong chelating agent and ensures an atomistical distribution of cations in the polymer structure.

As soon as added to the solution the sucrose gets hydrolyzed to fructose and glucose, which ultimately oxidizes to gluconic acid or a poly hydroxyl acid,

$$\begin{aligned} &C_{12}H_{22}O_{11}(\text{sucrose}) + H_2O \\ &\quad \rightarrow C_6H_{12}O_6(\text{glucose}) + C_6H_{12}O_6(\text{fructose}), \\ &C_6H_{12}O_6(\text{fructose}) \\ &\quad \rightarrow C_6H_{12}O_7(\text{gluconic acid}) \end{aligned} \tag{2}$$

Gluconic acid, with a carboxylic acid group in one end and five linear hydroxyl groups, easily forms the metal ion complex. It forms a branched polymer with PVA in water [25]. When dried the sample obtained with sucrose in presence of PVA in a small 10% amount results in a desirably crushable, fluffy powder. In addition to dispersing metal cations in a network structure, the polymer matrix serves as an internal fuel to decompose and burn out the sample spontaneously into a refined powder in Cr^{3+}/Cr^{4+} stabilized ZrO_2 nanoparticles.

3.2. Reconstructive decomposition and combustion in precursor

In order to get refined ZrO_2 particles in controlled size in few nanometers, the polymer precursor powder is first heated over a hot plate at low temperature as ~250°C. At this temperature, insufficient to induce its spontaneous combustion, it slowly disintegrates by a dynamic reconstructive organization of polymer molecules in small groups or particles in a self-controlled manner. As such the ZrO_2 ceramic components are encapsulated in thin surface layers of decomposed polymer molecules (mostly carbon) in a dark black color. At higher temperatures, the surface layer reacts with oxygen in air and goes away as oxidized gas species, leaving behind pure ZrO_2 ceramic particles in light brown to blue color as per the Cr^{3+}/Cr^{4+} additives. A continuous release of part of the material in a gas form from the surface layers (keep the particles separated apart) inhibits the particles to recombine and grow in a strictly controlled manner at 900°C or lower temperatures used in this example.

A reconstructive molecular decomposition of precursor at controlled combustion is highly effective to control size and/or morphology of final ZrO_2 particles. This is not possible by an adiabatic combustion process. For example, combustion of a precursor of metal cations dispersed in oxalic dihydrazide yields only a mixture of yttria stabilized c- and t-ZrO_2 in 1 to 5 μm particles [17]. No particles in a controlled nanometer size appear as obtained here as described below. As the metal salt and the organic compound act as oxidizing and reducing agents, respectively, a strong reduction-oxidation (redox) reaction takes place during the combustion. A large amount of heat and gas evolves rapidly in a very short period of time. The heat evolved leads the precursor to disintegrate instantaneously into refined particles and those succeed to recombine in rather big groups on highly reactive nascent surfaces. A large volume of gas produced does promote disintegration of precursor into small dispersed particles, but it lasts over a very limited period of time of a few seconds only and by the time most of the gas escapes and does not take an active part to inhibit recombination of particles even in a fast cooling after the combustion.

Fig. 3 shows (a) DTA and (b) TG curves in thermal decomposition and combustion in a continuous heating of 25 mg of polymer precursor (10 at.% Cr^{3+}/Cr^{4+} content and dried at 80°C over a water bath) at 5°C/min in air. A molecular decomposition with a predominant combustion occurs with an exothermic peak

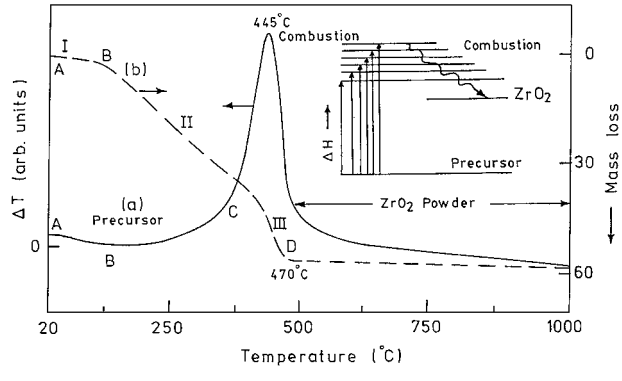

Figure 3 (a) DTA and (b) TG thermograms in a polymer precursor (with 10% Cr^{3+} and Cr^{4+} additives) dried over a water bath at 80°C. The data are collected by heating the sample at 5°C/min in air. A schematic diagram in thermal excitation of the precursor by absorption of enthalpy ΔH followed by dissociation and combustion is given in the inset.

TABLE II The total mass loss and structural H_2O in different precursors of zirconium hydroxide or oxyhydroxides

Precursor	x-value	Mass loss (%)	Reference
$ZrO(OH)_2$ anhydrate		12.8	
$ZrO(OH) \cdot xH_2O$ hydrate	1.0	22.6	Huang *et al.*[a]
$ZrO(OH) \cdot xH_2O$ gel	7.5	58.0	Present work
$Zr(OH)_4$ anhydrate		22.6	
Hydrous zirconia $ZrO_2 \cdot xH_2O$	1.9	21.5	Huang *et al.*
$ZrO(OH) \cdot xH_2O$-polymer (10 at.% Cr^{3+}/Cr^{4+})		59.0	Present work

[a]The data after Huang *et al.* in [30].

in combustion at $T_{PC} = 445°C$ in the DTA with a total $\Delta M = 59.0\%$ mass loss in the TG curve. As compared in Table II, a total 22.6% mass loss lies in $ZrO(OH)_2 \cdot H_2O \rightarrow ZrO_2 + 2H_2O$ molecular decomposition while 12.8% in the case of anhydrite $ZrO(OH)_2$ or 22.6% in anhydrite $Zr(OH)_4$. A hydrous zirconia, $ZrO_2 \cdot xH_2O$, $x \sim 1.9$, has 21.5% mass loss [30]. Thus the additional value in our polymer precursor imparts primarily from the polymer matrix with the structural H_2O molecules.

As marked over the TG curve (Fig. 3a), the mass loss in the polymer precursor proceeds in three successive steps I, II and III between the points of A, B, C and D. Signal I, which involves a very small $\Delta M \sim 2\%$ value and lasts to ~150°C, indicates desorption of part of H_2O and/or interstitial gases adsorbed during the processing. Generation of CO, CO_2 and NH_3 gases are common in processing of a polymer precursor with metal cations in an acidic medium in this example. Signal II has $\Delta M \sim 38\%$ and extends to 430°C while signal III, $\Delta M \sim 19\%$, lasts to point D at $T_{CC} \sim 470°C$. No further loss in mass appears in continuing the heating over higher temperatures above 470°C in air.

In principle, a desorption or decomposition is an endothermic process. It involves absorption of heat (or enthalpy ΔH) by excitation of the system through a series of energy levels (as shown in the inset to Fig. 3) in a molecular rearrangement to the limit of its thermodynamic stability from which it ultimately occurs. This is very much reflected in by desorption of the H_2O and interstitial gases in the endothermic signal I between points A and B (Fig. 3). Also the molecular decomposition of the polymer precursor at early temperatures in signal II begins with an altogether endothermic heat output in the DTA. A monotonically increasing rate of heat output leads to a spontaneous combustion of the sample in a prominent exothermic signal III at subsequent temperatures.

As portrayed in Figs 4 and 5, the values are decreasing in both T_{PC} and T_{CC} with an increasing value of Cr^{3+}/Cr^{4+} content (δ). Extrapolations of two curves to $\delta \rightarrow 0$ yield their maximal values of $T_{PC}^{m} = 465°C$ (Fig. 4) and $T_{CC}^{m} = 662°C$ (Fig. 5) in the virgin polymer with Zr^{4+} cations. The present values are as large as 52% of those of 385°C and 437°C, respectively, observed in the precursor with $\delta \sim 30\%$. The effect of δ in diminishing the final value in T_{PC} or T_{CC} seems to be the most prevalent at a specific value of it around 13%. In the T_{PC} vs. δ curve in Fig. 4, it thus reflects

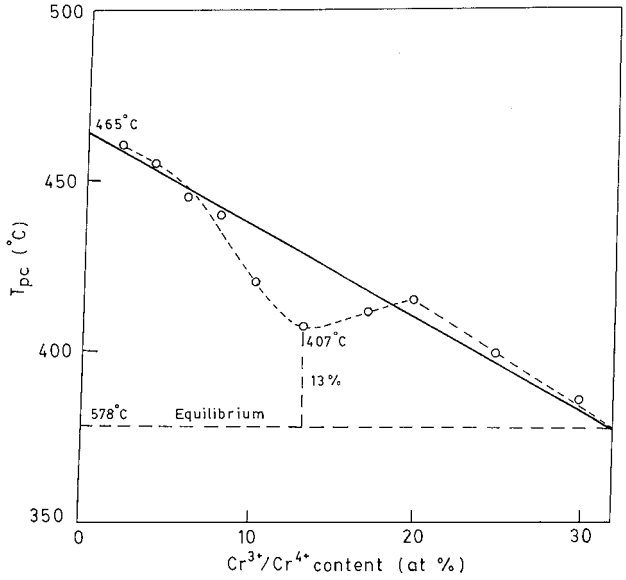

Figure 4 A plot of the exothermic peak temperature T_{PC} in DTA with a function of Cr^{3+}/Cr^{4+} content in the polymer precursor. Note the diminution in the T_{PC} value from 465°C to 378°C on adding the Cr^{3+} and Cr^{4+} in an amorphous polymer structure.

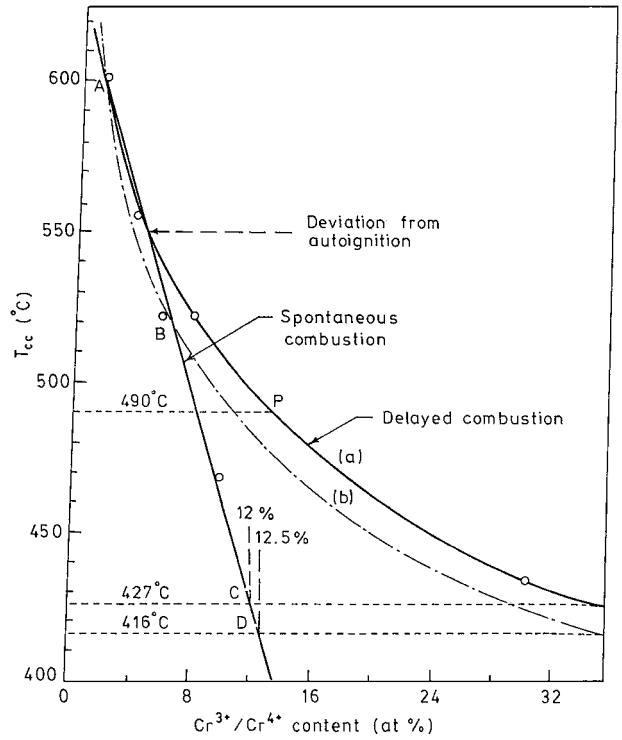

Figure 5 (a) A plot of complete combustion (constant weight) temperature T_{CC} in TG with a function of Cr^{3+}/Cr^{4+} content in the polymer precursor. Curve (b) is the simulation to that in (a). An extrapolation of a linear plot over the early data points of ABCD intersects their tangents at points C and D at (a) 12.0% and (b) 12.5% of Cr^{3+}/Cr^{4+} contents.

in a peak in T_{PC} at 407°C at this specific value. T_{CC} vs. δ curve, in Fig. 5, changes significantly in its slope at around this value ($T_{CC} \sim 490°C$) as marked therein by point P. In an inorganic precursor with hydrazine $(NH_2)_2 \cdot H_2O$ [20], Cr^{3+} additive is rather shown to improve the temperature of the recrystallization T_C into ZrO_2 nanoparticles. A large $T_C = 477°C$ value (which can be treated as our T_{PC}^{m} value) thus appears at $\delta = 5\%$ and that shifts further to 615 or 713°C at $\delta = 20$ or 30% [20].

A simulation to the experimental T_{PC} data points with a function of δ, i.e.

$$T_{PC} = f(\delta), \tag{3}$$

with

$$f(\delta) = T_{PC}(0) - \alpha\delta - \beta, \tag{4}$$

represents the results, qualitatively, at δ in the 0 to 0.30 range. Here, β is a parameter which governs an induced combustion in refined polymer molecules according to their thermal history developed at lower temperatures in heating as a function of temperature at a given rate. Obviously, it is operative only over a specific range of temperature (i.e., 415 to 440°C according to the observed data in Fig. 4) over which the polymer refines in smaller units in support of the Cr^{3+}/Cr^{4+} additives in process to the spontaneous combustion. If we ignore it, for a time being, the relation (3) simplifies to the equation of a straight line

$$T_{PC} = c - \alpha\delta \tag{5}$$

with the constant $c = T_{PC}$ (0), the value of T_{PC} at $\delta = 0$. It reproduces the results (shown by the solid line in Fig. 4) with $c = 465$°C and $\alpha = -5.3$°C per unit value of δ. In a realistic case, β is a function of temperature in the region in question such that it passes through a maximum in superposition with the straight line function to accord with the observed cure (marked by the dots). It can be ascribed in terms of an exponential function as often used to describe a first order phase transformation [31].

Similarly, an empirical exponential function,

$$T_{CC} = \gamma T_{CC}^{m} \exp -\left[\frac{F_{Cr}}{F_{Zr}}\right]^{n} + f\left(T_{CC}^{i}\right) \tag{6}$$

with F_{Cr} and F_{Zr} as the effective fractions of the Cr^{3+}/Cr^{4+} and Zr^{4+} cations in the polymer structure, may be used to ascribe the δ dependent T_{CC} in this example. It reproduces

$$T_{CC} = \gamma T_{CC}^{m} = T_{CC}^{m} \tag{7}$$

at $F_{Cr} = 0$ with $\gamma = 1$ the ideal value in the polymer before the Cr^{3+}/Cr^{4+} additives. The second term, $f(T_{CC}^{i})$, in Equation 6 describes a manifestation in the instantaneous T_{CC} value (which is denoted as T_{CC}^{i}) by the internal heating which initiates at a specific F_{Cr} and F_{Zr} combination. It is a complex function of T_{CC}^{i} which varies from the point to point according to the heat produced during the process and the average heat capacity. If it is assumed to be negligibly small relative to the first term, then the above relation simply reduces as

$$T_{CC} = \gamma T_{CC}^{m} \exp -\left[\frac{F_{Cr}}{F_{Zr}}\right]^{n} \tag{8}$$

Substituting the values for $F_{Cr} = \delta$ and $F_{Zr} = 1 - \delta$, in the assumption that all of the Cr^{3+}/Cr^{4+} and Zr^{4+} metal cations in the specimen formed a polymer structure with the PVA and sucrose polymer molecules, relation (8) represents

$$T_{CC} = \gamma T_{CC}^{m} \exp -\left[\frac{\delta}{1-\delta}\right]^{n} \tag{9}$$

It describes well the T_{CC} vs. Cr^{3+}/Cr^{4+} content plot in the solid curve a in Fig. 5. A best fit (the dashed curve b) to the experimental data appears assuming an empirical 0.95 value (which is not very off the ideal $\gamma = 1$ value) for the correlation constant γ with a value for the exponent $n = \frac{1}{2}$. A small difference in the two curves dictates the contribution of $f(T_{CC}^{i})$, especially in the high Cr^{3+}/Cr^{4+} contents above 10 at.%. It determines a so called "delayed combustion" of the precursor at manifested temperatures. This factor seems to be dominating in the case of the inorganic precursor with hydrazine so that the T_{CC} value increases with the function of Cr^{3+}/Cr^{4+} contents in an opposite trend as mentioned above. An extrapolation of a linear plot of the initial data points of ABCD intersects the tangents to the two curves a and b at points C and D at 12.0 and 12.5% of Cr^{3+}/Cr^{4+} contents, respectively. This straight line ABCD represents the Cr^{3+}/Cr^{4+} limited dynamics of T_{CC} in the spontaneous combustion of the precursor. A deviation from the experimental curve (a) starts in autoignition as early as at around 5% Cr^{3+}/Cr^{4+} additives.

The present model variations of the T_{CC} and T_{PC} values with the Cr^{3+}/Cr^{4+} contents demonstrate the fact that the metal cations impart the polymer structure of precursor and in turn influence the kinetics of (i) its combustion process and (ii) formation of stabilized ZrO_2 by reaction of its decomposed species of metal cations during the combustion. The Cr^{3+}/Cr^{4+} cations behave as an internal catalyst to facilitating the combustion at moderate temperature. This is the reason that they function as a stabilizing agent in forming stabilized ZrO_2 in refined particles at moderate temperature insufficient to induce their growth further by a surface diffusion controlled recombination reaction.

3.3. Phase analysis

Fig. 6 compares x-ray diffraction in (a) PVA polymer and the polymer precursors derived with Zr^{4+} metal cations with (b) 10 at.% and (c) 20 at.% Cr^{3+}/Cr^{4+} additives. All the three diffractograms are very similar with two broad halos at wavevectors in the range of $q_1 = 9$ to 12 nm^{-1} and $q_2 = 28$ to 30 nm^{-1} (defined by $q_i = 4\pi \sin\theta/\lambda$) in characteristics of their amorphous structures. Average positions in the derived polymer precursor have a marginal shift, as much as 3.1 nm^{-1}, in two halos in comparison to those in the virgin PVA or the PVA-sucrose polymers. This is expected in the predominant local structure of the PVA-sucrose

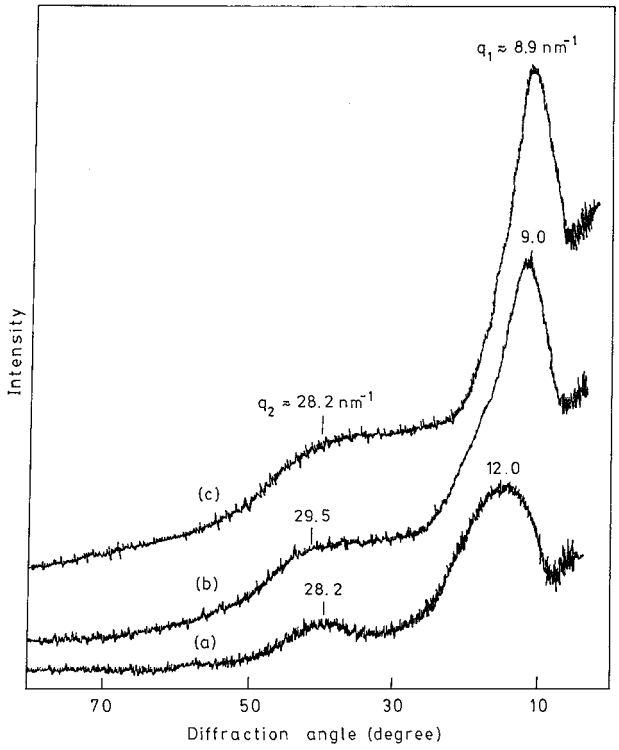

Figure 6 X-ray diffraction in (a) PVA polymer and the polymer precursors with Zr^{4+} metal cations with (b) 10 or (c) 20% Cr^{3+}/Cr^{4+} additives. A prominent halo q_1 appears at wavevector (a) 12.0, (b) 9.0, or (c) 8.9 nm^{-1} with a relatively weak halo q_2 at 28.2, 29.5, and 28.2 nm^{-1}, respectively.

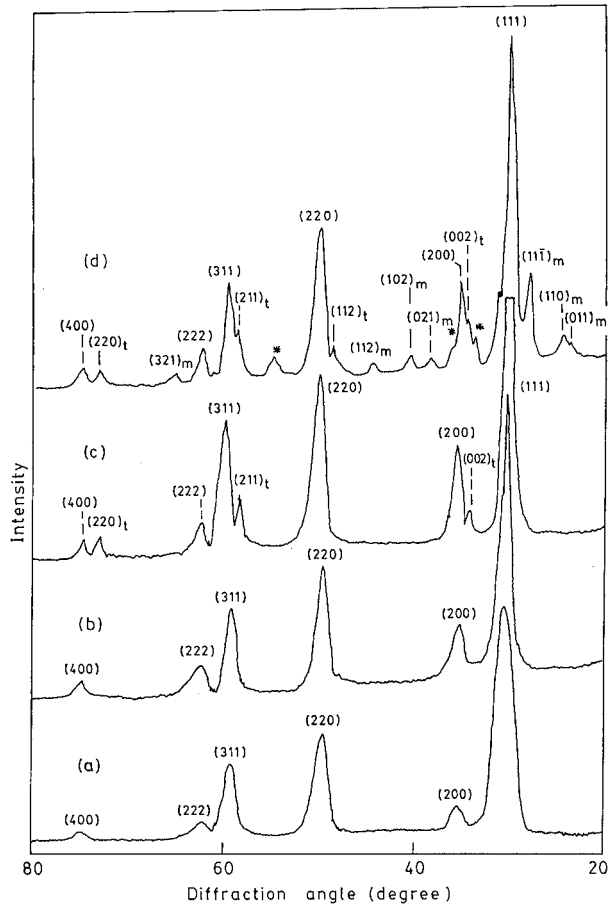

Figure 7 X-ray diffraction in stabilized ZrO_2 nanoparticles after calcining from the polymer precursor with 10% Cr^{3+}/Cr^{4+} at (a) 250, (b) 800, (c) 900, or (d) 950°C for 2 h. Part of c-ZrO_2 in (a) or (b) transforms to t-ZrO_2 in (c) while to t- and m-ZrO_2 in (d) as marked by (*hkl*) with subscript t or m. *h-Cr_2O_3.

polymer component in the final polymer precursor. Other details of the individual q_i values and bandwidths $\Delta 2\theta_{1/2}$ observed in the different samples are given in Table III.

A recrystallization from an amorphous precursor state results in stabilized ZrO_2 nanoparticles at 250 to 950°C. For example, Fig. 7 compares x-ray diffraction of stabilized ZrO_2 with 10% Cr^{3+}/Cr^{4+} additives by calcining the precursor at (a) 250, (b) 800, (c) 900, and (d) 950°C for 4 or 2 h. A single phase of c-ZrO_2 nanoparticles forms at 250 to 800°C in (a) and (b). The diffractogram is fairly matching the standard diffractogram in bulk c-ZrO_2 [32a]. Moreover, it is found that, on raising the temperature as 900°C in (c), part of the product converts into t-ZrO_2 nanoparticles, resulting in a composite microstructure of dispersed t-ZrO_2 nanoparticles in the matrix of c-ZrO_2 nanoparticles.

TABLE III Average positions (in wavevector in nm^{-1}) and bandwidths (in degree) in q_1 and q_2 x-ray diffraction halos in the virgin and derived PVA-sucrose polymer precursors

	Halo q_1		Halo q_2	
Sample	Position	Bandwidth	Position	Bandwidth
PVA polymer	12.0	14.0	28.2	10.0
PVA-sucrose polymer	12.0	13.0	28.2	10.0
Derived PVA-sucrose precursor (10 at.% Cr^{3+}/Cr^{4+})	9.0	10.0	29.5	15.0
Derived PVA-sucrose precursor (20 at.% Cr^{3+}/Cr^{4+})	8.9	8.0	28.2	18.0

This maintains a thermodynamic equilibrium structure of derived specimen at or below 900°C temperatures. No additives of Cr^{3+}/Cr^{4+} cations segregate in an independent crystalline phase, confirming that they are dissolved in a solid solution with c- or t-ZrO_2 in nanoparticles.

A part of solid state phase separation occurs in h-Cr_2O_3 nanoparticles (R3c hexagonal corundum crystal structure [32b]) along with a polymorphic transformation in m-ZrO_2 at expense of the c-ZrO_2 in nanoparticles on raising the temperature further at 950°C as in Fig. 7d. A similar result of h-Cr_2O_3 phase separation follows in a prolong heating at 900°C for 15 h or longer. The result envisages that the c-ZrO_2 nanoparticles have presumably nucleated and grown in a solid solution with Cr^{3+}/Cr^{4+} cations through a high energy amorphous state. The capacity of c-ZrO_2 to dissolve Cr^{3+}/Cr^{4+} in a solid solution varies with its size (determines an increased value of the total Gibb's free energy and in turn a manifested reactivity in small particles) and the temperature. Small c-ZrO_2 crystallites processed at effectively low temperature thus offer a manifested solubility of bulk particles. As a result, part of Cr^{3+}/Cr^{4+} precipitates on growth of supersaturated c-ZrO_2(ss) particles with Cr^{3+}/Cr^{4+} in heating at these temperatures. The reaction in an extended heating from

an amorphous polymer precursor at 900°C thus can be expressed as follows

$$\text{Amorphous precursor} \xrightarrow{900^\circ\text{C}} \begin{array}{l} \text{c-}ZrO_2\,(\text{ss}) \rightarrow \text{c-}ZrO_2 + \text{h-}Cr_2O_3, \\ \text{c-}ZrO_2 \rightarrow \text{t-}ZrO_2, \\ \text{t-}ZrO_2 + \text{h-}Cr_2O_3 \rightarrow \text{t-}ZrO_2\,(\text{ss}) \\ \hline \text{c-}ZrO_2 \rightarrow \text{t-}ZrO_2(\text{ss}) \end{array} \tag{10}$$

A phase transformation of t-ZrO_2(ss) → m-ZrO_2 + h-Cr_2O_3 occurs in extended heating to 15 h at 900°C. An increase in temperature above 900°C promotes it to appear in a single m-ZrO_2 phase with incipient growth of h-Cr_2O_3, $a = 0.4954$ and $c = 0.1358$ nm, in 2 h at 1050°C (Fig. 8). The lattice parameters of $a = 0.5140$ nm, $b = 0.5195$ nm, $c = 0.5305$ nm, and $\beta = 99°23$, calculated in $P2_1/c$ m-ZrO_2 structure with the observed peak positions (d_{hkl} interplanar spacings) in the diffractogram, are bit decreased by ~0.2% in comparison to the $a = 0.5148$ nm, $b = 0.5203$ nm, $c = 0.5316$ nm, and $\beta = 99°23'$ bulk values [32c]. It is feasible if part of Cr^{3+}/Cr^{4+} additives (of lower ionic radius of 0.076 (Cr^{3+}) or 0.069 (Cr^{4+}) nm relative to 0.086 nm in Zr^{4+} in octahedral sites [33]) retain in a solid m-ZrO_2 solution.

The Cr^{3+}/Cr^{4+} additives facilitate the reaction of forming t-ZrO_2(ss) if used in an effectively large amount of 20 at.%, or even more. A specimen of t-ZrO_2(ss) thus appears with h-Cr_2O_3 as early as in

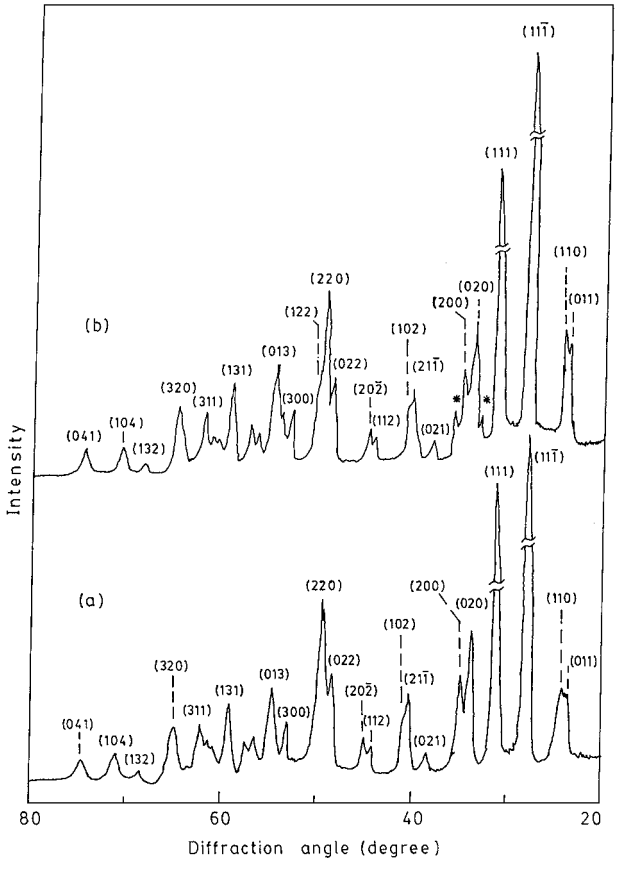

Figure 8 X-ray diffraction in phase transformation of c- or t-ZrO_2 into m-ZrO_2 with a differential h-Cr_2O_3 (*) separation at 1050°C in 2 h; (a) 10 or (b) 20% Cr^{3+}/Cr^{4+} contents.

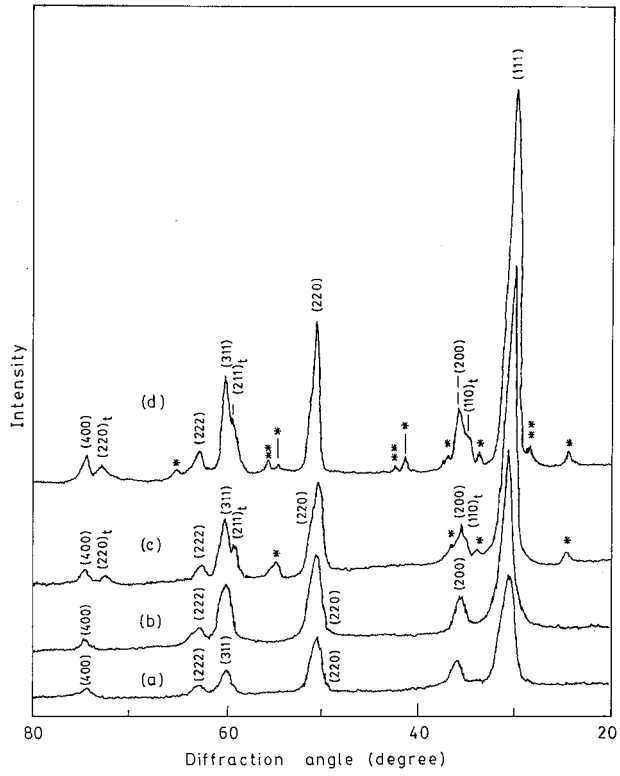

Figure 9 X-ray diffraction in stabilized ZrO_2 nanoparticles after calcining from the polymer precursor with 20% Cr^{3+}/Cr^{4+} at (a) 250, (b) 600, (c) 800, and (d) 900°C. Phase transformation from c-ZrO_2 to t-ZrO_2 starts with h-Cr_2O_3 (*) segregation at 800°C. ** t-CrO_2 appears at 900°C in (d).

2 h of heating at a relatively low 800°C temperature (Fig. 9). A new t-CrO_2 phase ($P4_2/mnm$ tetragonal structure [32d]) precipitates at temperature as high as 900°C. It converts to h-Cr_2O_3 in raising the temperature further as at 1050°C in Fig. 8. A content of Cr^{3+}/Cr^{4+} above 20 at.% is not so useful in preparing a solid ZrO_2 solution. It adds impurities of crystalline h-Cr_2O_3 even at lower temperatures as 250°C.

The present results differ from those of Cr^{3+} stabilized ZrO_2 recrystallized from an amorphous ZrO_2-Cr_2O_3 precursor via a precipitation reaction of the metal chlorides with hydrazine $(NH_2)_2 \cdot H_2O$ in water and then drying the recovered precipitate at 120°C under a reduced pressure [20]. In this case, t-ZrO_2 forms instead of c-ZrO_2 even at low 465 to 750°C temperatures by dissolving as much Cr_2O_3 as 20 at.%. At higher 900°C and above temperatures, the Cr^{3+} precipitates and the t-ZrO_2 converts into m-ZrO_2. A mixture in c- and m-ZrO_2 appears at larger Cr_2O_3 contents till 33 at.%. Cr^{4+} cations in combination with those of Cr^{3+} seems responsible in this example to stabilize c-ZrO_2 in a single phase in controlled size in few nanometers. As the results are summarized in Table IV, a pure c-ZrO_2 forms in support of 4 to 10 at.% Cr^{3+}/Cr^{4+} additives. They support an improved stability in c-ZrO_2 nanoparticles, especially in the presence of a minority phase of the other ZrO_2 polymorphs, so that they stand as such until the final temperature lies under 900°C.

The stabilized c-ZrO_2 with 1 at.% Cr^{3+}/Cr^{4+} additives in nanoparticles have a larger lattice parameter

TABLE IV The chemical compositions and experimental conditions of formation of Cr^{3+}/Cr^{4+} modified ZrO_2 in three polymorphs at different temperature from polymer precursors

Cr^{3+}/Cr^{4+} Content (at.%)	Heating		Identified ZrO_2 polymorphs
	Temp. (°C)	Time (h)	
0	250–500	2–4	c-ZrO_2, m-ZrO_2 (10)
	800	2	m-ZrO_2
2–4	250–800	2–4	c-ZrO_2, t-ZrO_2 (20), m-ZrO_2 (5)
5–10	250–800	2–4	c-ZrO_2
	900	2	c-ZrO_2, t-ZrO_2 (25)
	900	15	c-ZrO_2, t-ZrO_2 (30), m-ZrO_2 (20), h-Cr_2O_3
	950	2	c-ZrO_2, t-ZrO_2 (25), m-ZrO_2 (35), h-CrO_2
	1050	2	m-ZrO_2, h-Cr_2O_3
20	250–600	2–4	c-ZrO_2
	800	2	c-ZrO_2, t-ZrO_2 (35), h-Cr_2O_3
	900	2	c-ZrO_2, t-ZrO_2 (35), h-Cr_2O_3, t-CrO_2
	950	2	m-ZrO_2, c-ZrO_2 (20), t-ZrO_2 (10), h-Cr_2O_3
	1050	2	m-ZrO_2, h-Cr_2O_3
30	250–600	2–4	c-ZrO_2, h-Cr_2O_3
	800 to 1050	2	Same as with 20% Cr^{3+}/Cr^{4+} additives

The volume fractions (%) are given in the parentheses in the minority ZrO_2 phases according to the relative intensities in the characteristic x-ray diffraction peaks.

$a = 0.5130$ nm of pure sample of $a = 0.5090$ nm [32a]. An increase in the Cr^{3+}/Cr^{4+} content reflects in a bit decrease in the a value to 0.5070 nm at $\delta \sim 10$ at.% as per the c-ZrO_2 + $\delta Cr^{3+}/Cr^{4+} \rightarrow$ c-ZrO_2(ss) solid solution formation. It accords to an average smaller value of ionic radius in the Cr^{3+}/Cr^{4+} cations over that in the Zr^{4+} cations. Dissolution of Cr^{3+}/Cr^{4+} in t-ZrO_2 involves a maximum 1.0% decrease ($\delta \sim 10$ at.%) in $c = 0.5220$ nm and 0.28% in $a = 0.3630$ nm lattice parameters against $a = 0.5270$ and $c = 0.3640$ nm bulk values [32e]. No significant change occurs in the a value in stabilizing t-ZrO_2 by adding Cr^{3+} alone [20]. Possibly, it occupies the sites primarily along the c-axis.

In a composite sample, the volume fraction V_m in m-ZrO_2 nanoparticles dispersed in a matrix of c- and t-ZrO_2 may be estimated by the integrated intensities in the characteristic diffraction peaks I_i in the three phases with an empirical relation

$$V_m = \frac{\sum_{i=1}^{m} K_m (I_i)_m}{\sum_{i=1}^{m} K_m (I_i)_m + \sum_{i=1}^{n} K_t (I_i)_t + \sum_{i=1}^{0} K_c (I_i)_c} \quad (11)$$

The constants K_m, K_t and K_c correlate the fractional volumes V_m, V_t and V_c through the integrated intensities in the respective phases. The value of i varies over the total numbers of peaks m, n and p in the three phases, respectively. Assuming $K_t \sim K_c \cong \eta K_m$, in a close similarity in x-ray diffraction in t- and c-ZrO_2, Equation 11 simplifies

$$V_m = \frac{\sum_{i=1}^{m} (I_i)_m}{\sum_{i=1}^{m.n.o} [(I_i)_m + \eta\{(I_i)_t + (I_i)_c\}]} \quad (12)$$

or

$$V_m = \frac{1}{1 + \eta\{(I_{101})_t + (I_{111})_c\}\{(I_{111})_m + (I_{11\bar{1}})_m\}^{-1}} \quad (13)$$

assuming the partial I values in the prominent (111) and (11$\bar{1}$) peaks in m-ZrO_2 while (101) peak in t-ZrO_2 and (111) peak in c-ZrO_2. A numerical value obtained by the areas $(I_{111})_m$ and $(I_{11\bar{1}})_m$ in (111) and (11$\bar{1}$) peaks in m-ZrO_2, $(I_{101})_t$ in (101) peak in t-ZrO_2, and $(I_{111})_c$ in (111) peak in c-ZrO_2 satisfactorily reproduces V_m with an independently determined value of $\eta = 0.8$. The empirical $\eta = 0.8$ value used here has been analyzed with x-ray diffraction in known mixtures in three phases. As mentioned above, $\eta = 1$ is used to analyze V_c or V_t in the case of a binary c- and t-ZrO_2 mixture. The volume fractions thus obtained in the minor phases in the powders processed under different experimental conditions are given in Table IV.

Obviously, the above relation is very logical and realistic for a quantitative analysis of volume fractions in crystalline phases in a physical mixture or composite. It is very similar to the relation, as proposed earlier by Toraya *et al.* [34],

$$V_m = \frac{P X_m}{1 + (P - 1) X_m} \quad (14)$$

where

$$X_m = \frac{(I_{111})_m + (I_{11\bar{1}})_m}{(I_{111})_m + (I_{11\bar{1}})_m + (I_{101})_t + (I_{111})_c} \quad (15)$$

with an empirical 1.31 value for the correlation constant P to account for the nonlinearity in V_m as function of X_m. Our powder ($\delta = 10$ at.% and annealed 2 h at 950°C) in Fig. 7d, has a value of $X_m \sim 0.29$, which determines a value of $V_m = 35\%$ through Equation 14. An exactly the same value of $V_m = 35\%$ is obtained by application of Equation 13 developed in this work. Furthermore, as per peak intensity $I = 25\%$ (against $I = 20$ standard value) in (311) peak in c-ZrO_2 and $I = 13\%$ ($I = 15$ standard value) in (211) in t-ZrO_2, volume V_c in c-phase is as much as 1.5 times in t-phase.

3.4. Size and morphology in ZrO_2 nanoparticles

The Cr^{3+}/Cr^{4+} stabilized c-ZrO_2 in small crystallites or particles are in near spherical shapes. Their final morphology or size does not change much in processing by the polymer precursor at different temperatures in the 250 and 800°C range. For example, a TEM micrograph for a c-ZrO_2 nanopowder, processed with 10 at.% Cr^{3+}/Cr^{4+} at 250°C in 2 h, is given in Fig. 10a. Average diameter in small particles is $D \sim 6$ nm. The value hardly increased from the 6 nm to 10 nm on raising the temperature from the 250°C to 800°C. On a small increase in the temperature to 900°C, part of them rearrange locally and grow in a modified acicular morphology in phase transformed t-ZrO_2 (confirmed with *in situ* analysis of the electron diffraction). This is shown with TEM of a selected region of the specimen (processed 2 h at 900°C) in Fig. 10b. These t-ZrO_2 particles are as long as 450 nm in 15 to 30 nm widths with aspect ratio $\phi \leq 20$. Part of the particles, which are still in c-ZrO_2 phase, retain their original spherical shpaes with no much growth ($D \sim 10$ to 20 nm).

Average $d = 5$ to 10 nm crystallite size, calculated by $\Delta 2\theta_{1/2}$ in the x-ray diffraction peaks with the Debye-Scherrer relation [26], compares the average size observed in the TEM micrographs. A close similarity in the values obtained in the two methods envisages that the small particles in TEM are the single crystallites. A significant lattice strain in small crystallites accounts for a reasonably smaller d value calculated without a correction of its contribution in $\Delta 2\theta_{1/2}$.

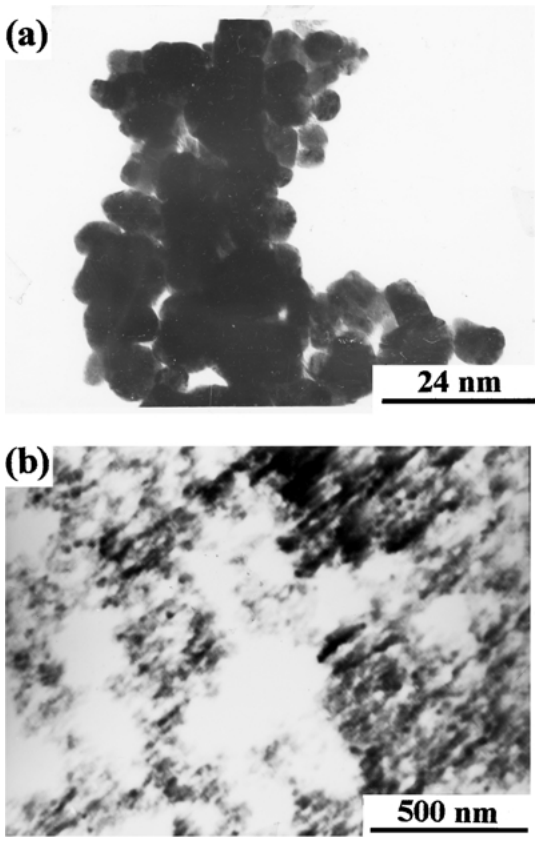

Figure 10 TEM micrograms in stabilized c-ZrO_2 or t-ZrO_2 nanoparticles with 10% Cr^{3+}/Cr^{4+} additives after calcining from the polymer precursor at (a) 250°C and (b) 900°C for 2 h.

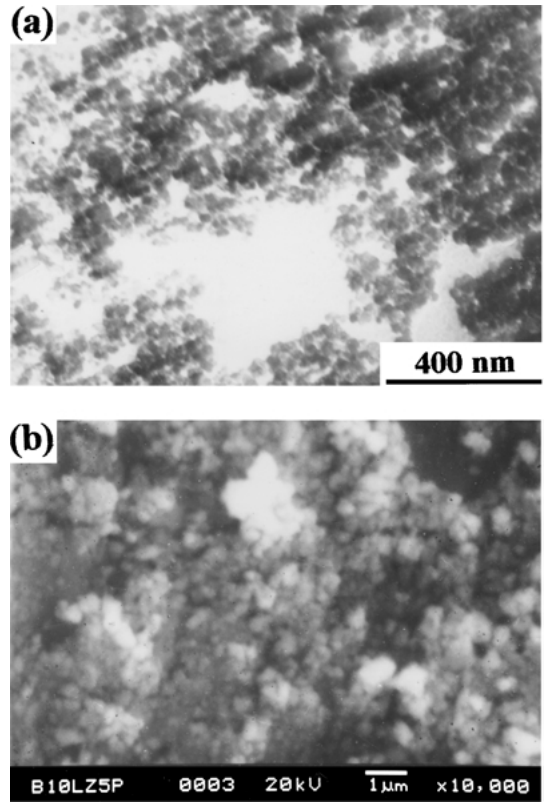

Figure 11 (a) TEM and (b) SEM micrograms in m-ZrO_2 nanoparticles or clusters with 10% Cr^{3+}/Cr^{4+} additives obtained after calcining from the polymer precursor at 1050°C for 2 h.

The crystallites in m-ZrO_2 form in an altogether different morphology in platelets or cubides in $d \sim 25$ nm (Fig. 11a) in heating from the polymer precursor at 1050°C for 2 h. They are arranged further in clusters of $D \sim 300$ nm average diameter. As many crystallites as $(D/d)^3 \sim 10^3$ are thus contained in a cluster in approximation of spherical shapes.

A spherical particle in radius $r = \frac{1}{2}D$ involves a specific surface area $A = 4\pi r^2 \div 4/3\ \pi r^3 \rho \equiv 3/r\rho$, where ρ is its density. Thus a value of $A \sim 200$ m^2/g (in comparison to the 180 m^2/g observed from the BET measurements) is calculated for a particle of $r = 2.5$ nm with $\rho = 6.10$ g/cm^3. It is as large as 4 times the value in a cluster of $D \sim 20$ nm. Assuming a close packing of particles in cluster and neglecting the interparticle space, a $D \sim 20$ nm cluster consists of a roughly 64 crystallites of $r = 2.5$ nm. At moderate 800°C or lower temperature, insufficient to cause a significant grain growth, ZrO_2 particles with so large A values configure in clusters in order to optimizing their equilibrium A_0 value. Their spherical shape is a consequence of optimization of their final morphology with a minimal A value. This, in turn, optimizes the total energy of the system to its equilibrium bulk value ε_0. This is the reason that the observed A value lies to be smaller than the calculated ones. The other details are given in Table V for the particles derived in three ZrO_2 polymorphs with 10 at.% Cr^{3+}/Cr^{4+} additives.

A large A-value determines a large value of the total surface Gibb's free energy $\Omega = A\sigma$, with σ the surface energy density, in small particles. As a result, a specimen of small particles has a huge value of the

TABLE V Average crystallite size d, surface area A, and apparent color in modified ZrO_2 nanoparticles with 10 at.% Cr^{3+}/Cr^{4+} additives at different temperatures

Sample	Color	Structure	d (nm)[a]	A (m^2/g)[b]
1. Dried precursor mass	Black	Amorphous		
2. Sample 1 pyrolysed at 250°C	Light yellow-brown	c-ZrO_2	5 (5–10)	180 (200)
3. Sample 2 annealed 2 h at 600–800°C	Light yellow-brown	c-ZrO_2	8 (5–12)	100 (130)
4. Sample 2 annealed 2 h at 900°C	Light yellow-blue	c- and t-ZrO_2	10 (10–30)	90 (100)
5. Sample 3 annealed 15 h at 900°C	Light blue	c-, t- and m-ZrO_2	15 (15–30)	55 (65)
6. Sample 3 annealed 2 h at 950°C	Light blue	c-, t- and m-ZrO_2	15 (15–30)	55 (65)
7. Sample 2 annealed 2 h at 1050°C	Light blue	m-ZrO_2	25 (20–40)	35 (40)

[a]Average d value calculated from the x-ray diffraction peakwidths. The observed particle size from TEM is compared in the parentheses. Crystallites are arranged in clusters or particles.
[b]The value calculated in the spherical shape of crystallites is given in the parentheses.

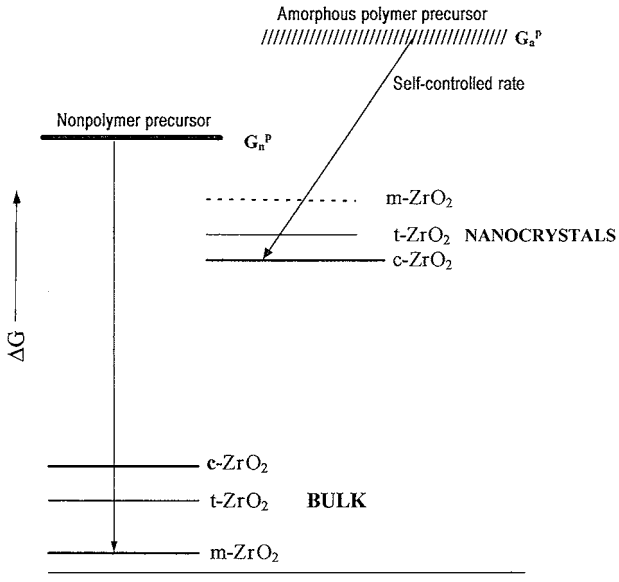

Figure 12 A schematic Gibb's free energy level diagram in three polymorphs in bulk and ZrO_2 nanocrystals. The high-energy nanoparticles appear in metastable c- and t-ZrO_2 polymorphs in processing from an energized amorphous state in a further higher-energy value.

total Gibb's free energy G above the equilibrium bulk value. This is demonstrated schematically in Fig. 12 in small particles and the bulk ZrO_2 in the three polymorphs. According to thermodynamics, an amorphous polymer precursor G_a^P as well as a nonpolymer precursor G_n^P has a further larger value of the Gibb's free energy as included in this figure. This is necessary in order to operate a phase transformation from it to one of the three polymorph states by releasing the excess structural energy by heating at an elevated temperature. The results are helpful in understanding the process of the formation and existence of the high energy c- and t-ZrO_2 metastable polymorphs in small particles with an adequate doping (increases the volume Gibb's free energy).

3.5. Optical spectra in Cr^{3+}/Cr^{4+} stabilized ZrO_2 nanoparticles

Part of Cr^{4+} in stabilized ZrO_2 nanoparticles is analyzed by the chemical tests as applied in Section 3.1 for the precursor solution in the virgin metal cations. In this case, 0.1 g of KI followed by 5.0 ml of CH_3COOH is added to a suspension of 0.2 g of the ZrO_2 sample in 20 ml of distilled water. A reaction of Cr^{4+} occurs with KI by releasing I_2 gas, $I^- + Cr^{4+} \rightarrow I_2 + Cr^{3+}$, which turns in a violet color of the specimen from a light green in the beginning. The acidic acid prevents Cr^{4+} oxidation with air and facilitates the reaction with iodide. An intense blue color appears on adding starch. It disappears if adding sodium thiosulphate.

The Cr^{4+} ($3d^2$) in c-ZrO_2 nanoparticles exhibits its characteristic absorption bands over 250 to 600 nm. As shown in Fig. 13, three distinct bands (marked by asterisks) appear at 558 ($^3T_1 \rightarrow {}^3A_2$), 421 ($^3T_1 \rightarrow {}^3T_1$), and 308, 293, 270 nm ($^3T_1 \rightarrow {}^3T_2$) in spectrum (a) for sample processed with 2 at.% Cr^{3+}/Cr^{4+} additives at 250°C. On incensing the Cr^{3+}/Cr^{4+} contents to 5 or 20 at.%, these bands shift at longer wavelengths by as much as 35 nm in spectra (b) and (c). The bands

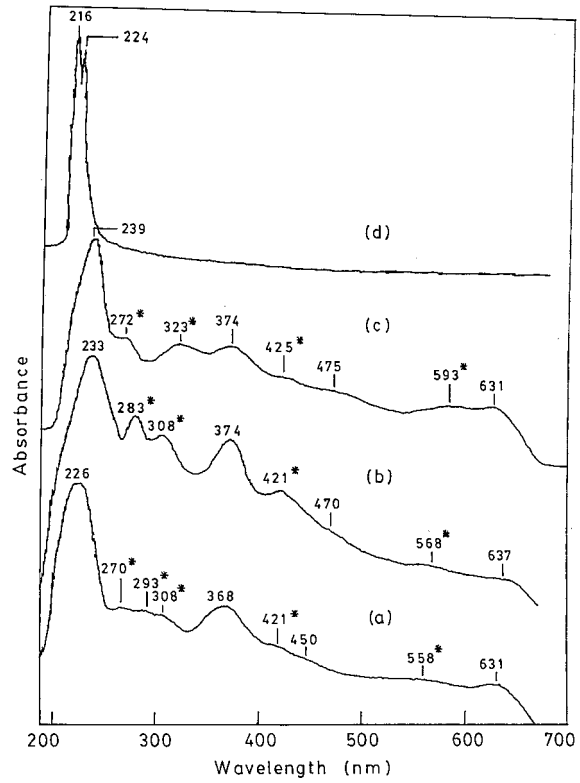

Figure 13 Electronic absorption spectra in stabilized c-ZrO_2 nanoparticles with (a) 1.0, (b) 5.0, and (c) 20% Cr^{3+}/Cr^{4+} additives. The sample had been calcined at 250°C for 4 h in (a) or (b) while at 800°C for 2 h in (c) following the polymer precursor. Spectrum (d) is from a specimen of pure m-ZrO_2 processed at 1000°C in 2 h without an additive in a similar method with a polymer precursor.

TABLE VI The electronic absorption bands (in nm) in the Cr^{3+}/Cr^{4+} doped c-ZrO_2 nanoparticles

Cr^{3+}/Cr^{4+} content (at.%)				
1	5	20	Pure m-ZrO_2	Transitions
631 (vw)	637 (vw)	631 (w)		$^4A_{2g} \rightarrow {}^2E_g$ (Cr^{3+})
558 (vw)	568 (vw)	593 (vw)		$^3T_1 \rightarrow {}^3A_2$ (Cr^{4+})
450 (vw)	470 (vw)	475 (vw)		$^4A_{2g} \rightarrow {}^4T_{2g}$ (Cr^{3+})
421 (w)	421 (w)	425 (w)		$^3T_1 \rightarrow {}^3T_1$ (Cr^{4+})
368 (ms)	374 (ms)	374 (ms)		$^4A_{2g} \rightarrow {}^4T_{1g}$ (Cr^{3+})
308 (w)	308 (w)	323 (w)		$^3T_1 \rightarrow {}^3T_2$ (Cr^{4+})
293 (w)	283 (ms)	–		
270 (w)	–	272 (ms)		Optical bandgap
226 (vs)	233 (vs)	239 (vs)	224 (s)	
			216 (vs)	

Relative band intensities are given in the parentheses; vs: very strong, s: strong, ms: medium strong, w: weak, and vw: very weak intensity values.

The samples of 1 or 5 at.% Cr^{3+}/Cr^{4+} have been processed at 250°C in 4 h while that of 20 at.% Cr^{3+}/Cr^{4+} at 800°C in 2 h. The pure m-ZrO_2 has been processed at 1000°C in 2 h.

which appear in $Cr^{3+}(3d^3)$ at 631 ($^4A_{2g} \rightarrow {}^2E_g$), 450 ($^4A_{2g} \rightarrow {}^4T_{2g}$), and 368 nm ($^4A_{2g} \rightarrow {}^4T_{1g}$) in (a) shift at 637, 470 and 374 nm in (b) while at 631, 475 and 374 nm in (c). A sample (m-ZrO_2) without any additive has a strong doublet bond group of two bands at 216 and 224 nm in spectrum (d) in electronic excitation through its optical gap [35]. A single unresolved band occurs at (a) 226, (b) 233 and (c) 239 nm in Cr^{3+} and Cr^{4+} stabilized c-ZrO_2 nanoparticles. Other details with the assignments of the individual bands observed in the representative samples are given in Table VI.

In general, the electronic bands in the Cr^{4+} cations are enriched in intensity to almost equal to those in Cr^{3+} in increasing the total Cr^{3+}/Cr^{4+} contents from (a) 2 to (b) 10 to (c) 20 at.%. The processing temperature is 250°C in (a) or (b) while 800°C in (c). The c-/t-ZrO_2 crystallites, $d \sim 8$ nm, in (c) are grown almost twice as big those of the c-ZrO_2 in (a) or (b). The present result infers the $Cr^{3+} \rightarrow Cr^{4+}$ transformation upon grain growth in stabilized c-/t-ZrO_2 in nanoparticles. As also evident by the x-ray diffraction, part of the Cr^{4+} cations participate in growth of stabilized ZrO_2 nanoparticles by partially substituting the Zr^{4+} sites in the lattice. It appears that part of the Cr^{3+} cations used in the precursor form a thin amorphous surface layer over individual crystallites and thus help in forming the stable ZrO_2 crystallites with stabile surfaces. The presumed grain surface layer inhibits a moderate grain growth and thus results in formation of small ZrO_2 crystallites at 900°C or lower temperatures.

A grain surface layer of additives in thickness Δr over a spherical particle of radius r imparts a volume fraction

$$f = \frac{4\pi r^2 \Delta r}{\frac{4}{3}\pi r^3 + 4\pi r^2 \Delta r} = \frac{3\Delta r}{r + 3\Delta r} \qquad (16)$$

Assuming 50 to 80% of the total Cr^{3+}/Cr^{4+} cations to be consumed in forming a uniformly distributed grain surface layer, a ZrO_2 sample stabilized with 10 at.% Cr^{3+}/Cr^{4+} additives would have $f = 5$ to 8%, which gives a value of the $\Delta r = 0.10$ to 0.15 nm at $r = 5$ nm. Roughly, it involves 1 to 2 molecular Cr_2O_3/CrO_2 layers, which are sufficient enough to form a thermodynamically rigid and stable grain surface in combination with the other surface cations or molecules in individual ZrO_2 nanoparticles.

4. Conclusions

A novel chemical method is explored with a polymer precursor for synthesizing stabilized ZrO_2 nanoparticles with an additive of Cr^{3+} and Cr^{4+} in a single metastable c-ZrO_2 phase or in a nanocomposite with t- and/or m-phase(s). It involves synthesis of a high energy precursor of dispersed Zr^{4+}, Cr^{3+} and Cr^{4+} metal cations in a polymer of sucrose and polyvinyl alcohol. The polymer molecules offer two important functions of (i) a solid dispersoid and (ii) a solid fuel. An aqueous solution of the polymer dissolves the metal cations (through aqueous solutions) in a transparent homogenous polymer solution at room temperature. It results in an amorphous polymer precursor powder on evaporating the excess water at 50 to 80°C. A refined nanopowder appears in stabilized c-ZrO_2, with as small as $d = 5$ nm controlled crystallite size of spherical shape, on heating from the precursor at temperature as low as $T_P \sim 250$°C in air. It transforms to t-ZrO_2 on a prolong annealing of 12 h at 900°C. Peculiarly, the t-ZrO_2 has an acicular shape of particles as long as 450 nm in 15 to 30 nm widths and $\phi \leq 20$ aspect ratio. Clusters of small $d \sim 25$ nm crystallites form in a single m-ZrO_2 phase at as early temperature as 1050°C in 2 h. They are grown to as big as in $D \sim 300$ nm diameter.

X-ray diffraction show a structure of a solid solution in stabilized c-ZrO_2 nanoparticles with 4 to 10% Cr^{3+}/Cr^{4+} additives. No precipitate occurs in an independent crystallite phase in the additives as long as the temperature lies under 800°C. At early dissolution of $Cr^{3+}/Cr^{4+} \sim 2$ at.%, the sample suffers with a significant lattice expansion with lattice parameter $a = 0.5130$ nm over the 0.5090 nm value in the pure sample. A further addition of Cr^{3+}/Cr^{4+} reflects in a decrease in the a value (up to 0.5070 nm at 10% additive) as per a c-ZrO2 + $\delta Cr^{3+}/Cr^{4+} \rightarrow$ c-ZrO_2 (ss) solid solution formation. A smaller ionic radius of 0.076 nm in Cr^{3+} or 0.069 in Cr^{4+} over 0.086 nm in Zr^{4+} accounts for the decrease in a value on their dissolution. Cr^{3+}/Cr^{4+} dissolution in t-ZrO_2 involves an optimal 1.0% decrease (at $\delta \sim 10\%$) in $c = 0.5220$ nm and 0.28% in $a = 0.3630$ nm value. No significant change occurs in a value if dissolving Cr^{3+} alone [20], possible if it occupies the sites primarily along the c-axis.

The optical absorption spectra reveal as small fraction of Cr^{4+} as half the Cr^{3+} in amorphous, or recrystallized precursor in $d \sim 5$ nm ZrO_2 crystallites, with an effectively sufficient amount of $\delta \sim 10\%$ to stabilize the metastable c- or t-phase. Its content increases with grain growth in stabilized ZrO_2 at expense of Cr^{3+} at grain surface. An almost equal fraction results in Cr^{4+} and Cr^{3+} at effectively large 8–10 nm crystallites. It is possible if Cr^{4+} substitutes in part of Zr^{4+} in the crystal lattice while Cr^{3+} forms a thin grain surface layer with

Zr^{4+} in small ZrO_2 crystallites. A stable grain surface with a thin amorphous surface layer, in 1 to 2 molecular layers of thickness, effectively controls the grain growth in small crystallites. Surface area does not drop below 55 m^2/g until the temperature is raised above 900°C.

Acknowledgments

This work has been financially supported by the Council of Scientific & Industrial Research (CSIR), Government of India.

References

1. R. C. GARVIE, R. H. HANNINK and R. T. PASCOE, *Nature* **258** (1975) 703.
2. R. H. J. HANNINK, P. M. KELLY and B. C. MUDDLE, *J. Amer. Ceram. Soc.* **83** (2000) 461.
3. S. FABRIS, A. T. PAXTON and M. W. FINNIS, *Phys. Rev.* B **62** (2000) 6617.
4. S. OSTANIN, A. J. CRAVEN, D. W. McCOMB, D. VLACHOS, A. ALAVI, M. W. FINNIS and A. T. PAXTON, *ibid.* **62** (2000) 14728.
5. K. MATSUI and M. OHGAI, *J. Amer. Ceram. Soc.* **84** (2001) 2303.
6. D. M. ADAMS, S. LEONARD, D. R. RUSSELL and R. J. CERNIK, *J. Phys. Chem. Solids* **52** (1991) 1181.
7. J. E. LOWTHER, *Phys. Stat. Solidi* (b) **217** (2000) 533.
8. M. Z. C. HU, R. D. HUNT, E. A. PAYZANT and C. R. HUBBARD, *J. Amer. Ceram. Soc.* **82** (1999) 2313.
9. S. RAGHAVAN, H. WANG, W. D. PORTER, R. B. DINWIDDIE and M. J. MAYO, *Acta Mater.* **49** (2001) 169.
10. D. XIAMING, LI QINGFENG and T. YUYING, *J. Amer. Ceram. Soc.* **76** (1993) 760.
11. K. ISHIDA, K. HIROTA, O. YAMAGUCHI, H. KUME, S. INAMURA and H. MIYAMOTO, *ibid.* **77** (1994) 1391.
12. T. TSUKADA, S. VENIGALLA, A. A. MORRONE and J. H. ADAIR, *ibid.* **82** (1999) 1169.
13. B. XIA, L. DUAN and Y. XIE, *ibid.* **83** (2000) 1077.
14. G. L. MESSING, SHE-CHANG ZHANG and G. V. JAYANTHI, *ibid.* **76** (1993) 2707.
15. G. SKANDAN, H. HANN, M. RODDY and W. R. CANNON, *ibid.* **77** (1994) 1706.
16. Y. XIE, *ibid.* **82** (1999) 768.
17. K. R. VENKATACHARI, D. HUANG, S. P. OSTRANDER, W. A. SCHULZE and G. C. STANGLE, *J. Mater. Res.* **10** (1995) 748.
18. M. JAYRATNA and M. YOSHIMURA, *J. Mater. Sci.* **21** (1986) 591.
19. P. LI, I. W. CHEN and J. E. P. HAHN, *J. Amer. Ceram. Soc.* **77** (1994) 118.
20. S. HIRANO, M. YOSHINAKA, K. HIROTA and O. YAMAGUCHI, *ibid.* **79** (1996) 171.
21. G. STEFANIC, S. POPOVIC and S. MUSIC, *Mater. Lett.* **36** (1998) 240.
22. N. Q. MINH, *J. Amer. Ceram. Soc.* **76** (1993) 563.
23. W. WEN-XIANG, L. ZHENG and LI FAN, *J. Solid State Chem.* **107** (1993) 201.
24. A. H. HEUER, N. CLAUSSEN, W. M. KRIVEN and M. RUHLE, *J. Amer. Ceram. Soc.* **65** (1982) 461.
25. J. C. RAY, P. PRAMANIK and S. RAM, *Mater. Lett.* **48** (2001) 281.
26. M. P. KLUG and L. E. ALEXANDER, "X-ray Diffraction Procedure for Polycrystalline and Amorphous Materials" (Wiley, New York, 1974) p. 634.
27. P. MOHANTY and S. RAM, *Phil. Magn.* B **82** (2002) 1129.
28. D. F. SHRIRER, P. W. ATKINS and C. H. LANGFORD, "Inorganic Chemistry" (Wiley, New York, 1990) p. 434.
29. S. RAM, K. RAM and B. S. SHUKLA, *J. Mater. Sci.* **27** (1992) 511.
30. C. HUANG, Z. TANG and Z. ZHANG, *J. Amer. Ceram. Soc.* **84** (2001) 1637.
31. S. RAM, *Phys. Rev.* B **49** (1994) 9632–38.
32. X-ray powder diffraction JCPDS File (a) 27.997, c-ZrO_2, (b) 6.054, h-Cr_2O_3, (c) 13.307, m-ZrO_2, (d) 9.0332, t-CrO_2, and (e) 24.1164, t-ZrO_2.
33. R. D. SHANNON, *Acta Cryst.* A **32** (1976) 751.
34. H. TORAYA, M. YOSHIMURA and S. SOMIYA, *J. Amer. Ceram. Soc.* **67** (1984) 119.
35. I. KOSACKI, V. PETROVSKY and H. U. ANDERSON, *Appl. Phys. Lett.* **74** (1999) 341.

Received 12 July
and accepted 31 October 2002